

Event driven 4D STEM acquisition with a Timepix3 detector: microsecond dwell time and faster scans for high precision and low dose applications

D. Jannis^{a,b}, C. Hofer^{a,b}, C. Gao^{a,b}, X. Xie^{a,b}, A. Béché^{a,b}, T.J. Pennycook^{a,b}, J. Verbeeck^{a,b,*}

^aEMAT, University of Antwerp, Groenenborgerlaan 171, 2020 Antwerp, Belgium

^bNANOLab Center of Excellence, University of Antwerp, Groenenborgerlaan 171, 2020 Antwerp, Belgium

Abstract

Four dimensional scanning transmission electron microscopy (4D STEM) records the scattering of electrons in a material in great detail. The benefits offered by 4D STEM are substantial, with the wealth of data it provides facilitating for instance high precision, high electron dose efficiency phase imaging via center of mass orptychography based analysis. However the requirement for a 2D image of the scattering to be recorded at each probe position has long placed a severe bottleneck on the speed at which 4D STEM can be performed. Recent advances in camera technology have greatly reduced this bottleneck, with the detection efficiency of direct electron detectors being especially well suited to the technique. However even the fastest frame driven pixelated detectors still significantly limit the scan speed which can be used in 4D STEM, making the resulting data susceptible to drift and hampering its use for low dose beam sensitive applications. Here we report the development of the use of an event driven Timepix3 direct electron camera that allows us to overcome this bottleneck and achieve 4D STEM dwell times down to 100 ns; orders of magnitude faster than what has been possible with frame based readout. We characterise the detector for different acceleration voltages and show that the method is especially well suited for low dose imaging and promises rich datasets without compromising dwell time when compared to conventional STEM imaging.

Keywords: Scanning transmission electron microscopy, 4D STEM, Low dose, Event based detection

1. Introduction

The development of direct pixelated detectors has revolutionized the imaging capabilities of multiple scientific fields, from particle tracking to X-ray and electron microscopy [1, 2]. In electron microscopy (EM), the efficiency of direct detectors has provided a leap forward in the dose efficiency possible in transmission electron microscopy (TEM). For fields such as molecular biology the resolution provided by EM is limited more by the poor signal achievable using the extremely low doses required to avoid unacceptable damage to the material than by the electron optics themselves. For such fields therefore dose efficiency is of the utmost importance, and the greatly enhanced dose efficiency provided by direct electron detectors made possible the so called resolution revolution in cryo-EM [3, 4].

The most fragile dose sensitive samples, such as proteins, have largely been the preserve of conventional

phase contrast TEM imaging as in cryo-EM. Phase contrast imaging in STEM has historically been far less dose efficient, but advanced STEM methods that also provide highly dose efficient phase contrast signals have been developed and also benefited greatly from advances in pixelated detector technology [5]. The vastly expanded information on the position dependence of the electron scattering provided in 4D STEM by capturing a 2D image of the scattering at each probe position provides advantages that go well beyond the much greater flexibility it provides in choosing between conventional STEM imaging modalities after taking the data [6, 7]. The richness of 4D STEM datasets also allow for significantly more advanced analysis. For example, center of mass (COM) andptychographic based 4D STEM methods both provide greatly enhanced sensitivity to the local potentials of a material and greatly enhanced signal per electron compared to conventional STEM methods [8, 6, 9]. Moreoverptychographic methods have been shown capable of also providing significantly enhanced dose efficiency over conventional TEM phase contrast [10], thus offering the prospect of

*Corresponding author

Email address: jo.verbeeck@uantwerp.be (J. Verbeeck)

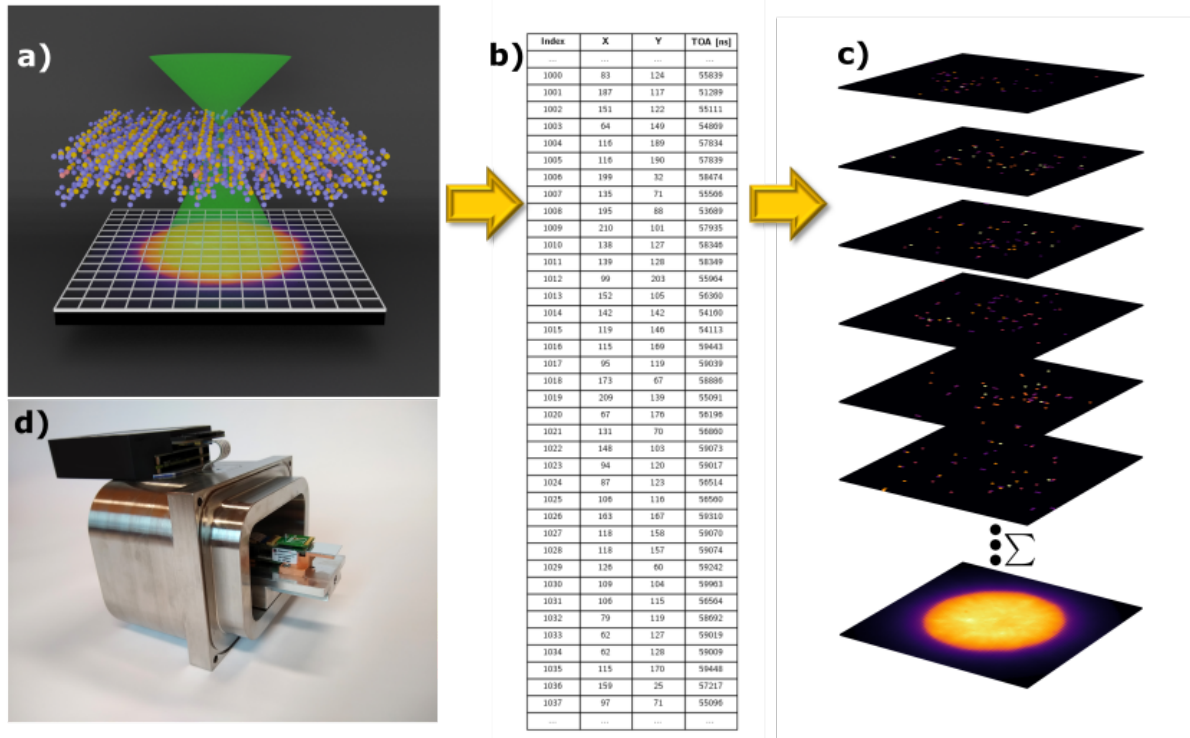


Figure 1: (a) The schematic setup, where a convergent electron beam is scanned across the sample and during the scan, the point of impact and TOA is measured for each incoming electron. (b) The data list created by the detector where for every event the point of impact and TOA is indicated. (c) When the probe position at each time is accurately known, a diffraction pattern belonging to the time range for a given probe position can be obtained resulting in a full 4D STEM dataset. (d) Custom built retractable assembly to place the Timepix3 detector in the electron microscope column.

another leap forward in low dose performance as well as a greater precision, for example for mapping local charge densities[11, 12, 13].

4D STEM methods such as COM or ptychography do not require cameras with particularly large numbers of pixels [9, 14]. Given the achievable frame rate depends on the number and bit depth of the pixels due to finite readout and data transfer rates, the development of small direct electron detectors has greatly benefited 4D STEM. Small fast hybrid pixel direct electron detectors such as the Medipix3 [15] are particularly attractive as they also offer the benefit of beam hardness, with the detection layer physically separated from the readout electronics. However, such detectors have typically been employed at frame rates of at most a few thousand frames per second [16].

By utilizing the much reduced bandwidth required for a 1-bit counting depth in each pixel of a Medipix3 detector, O’Leary et al. demonstrated a significant speedup of 4D STEM acquisition at a 12.5 kHz frame rate, corresponding to an 80 microsecond dwell time [17]. Al-

though this allowed them to achieve a relatively low dose of $200 \text{ e}^- \text{ \AA}^{-2}$ by using an extremely low probe current in a focused probe configuration, such a dose is still much higher than required by the most beam sensitive materials and the speed is still far slower than the single to few microsecond dwell times used in rapid conventional ADF based STEM measurements. Detector technology continues to advance and achievable frame rates are increasing. For example 11 microsecond dwell time 4D STEM has recently been achieved with a specially designed custom extremely high frame rate camera [18, 19], but this is still an order of magnitude slower than typical for rapid scanning STEM.

By using a defocused probe the CBED pattern contains information from a larger area of the sample from each probe position. Although significant overlap of the illuminated sample areas from adjacent probe positions is generally required, the reduced real space sampling requirements allows defocused probe ptychography techniques [20, 21] to more easily reach low doses with relatively slow cameras compared to focused probe

techniques. This advantage has recently been utilized to demonstrate defocused probe electron ptychography at extremely low cryo-EM doses with a Medipix3 [22], showing advantages over conventional TEM common to ptychographic techniques such as the single signed contrast transfer function (CTF) with a passband optimizable via the convergence angle and without the need for additional aberrations. However defocused probe techniques preclude the simultaneous use of the highly informative ADF based Z-contrast signal and generally involve solving for the phase using iterative convergence with the accompanying risks of incorrect convergence particularly at low doses. The focused probe single side band (SSB) [23, 6] and the Wigner distribution deconvolution (WDD) [24, 25] methods can provide simultaneous Z-contrast signals and non-iterative phase determination, and with progressing camera speedup can also now reach the extreme low dose regime of cryo-EM.

Here we demonstrate the use of an alternative event driven detector architecture to completely remove the bottleneck in speed for 4D STEM in comparison to conventional STEM detectors based on scintillators and photomultipliers for the low probe currents desirable for low dose operation. The event driven Timepix3 detector was developed with an emphasis on time resolution for applications in a wide range of scientific disciplines with a maximum time resolution of 1.56 ns [26, 27]. Event driven operation allows one to take advantage of event sparsity to achieve enhanced time resolution by avoiding the readout of pixels containing zero counts. In STEM one can reduce the dose imposed on a sample per unit area by reducing the probe current and dwell time, both of which increase the sparsity of the events in each probe position. We present results from 4D STEM performed with a Timepix3 detector at dwell times of a few microseconds down to 100 ns at both 60 and 200 kV accelerating voltages. Although the detector configuration used herein requires the use of low probe currents, we show how the speed facilitates multiply scanned 4D STEM to be used in order to increase the signal-to-noise with minimal susceptibility to drift. The results demonstrate that event driven camera technology enables the efficiency of 4D STEM and in particular electron ptychography to be exploited for both large fields of view and the extremely low doses without resorting to a defocused probe configuration.

2. Experimental Setup

The event based detector used in the camera setup in this work is the AdvAPIX TPX3 [28] which is a

Timepix3 based detector where the thickness of the sensitive silicon layer is 300 μm . Timepix3 chips are 3-side tileable with a maximum event capacity of $0.43 \times 10^6 / \text{mm}^2 / \text{s}$. A single Timepix3 chip contains 256×256 pixels where each pixel has a size of $55 \times 55 \mu\text{m}$, resulting in a theoretical capacity of 80×10^6 counts per second for a single chip device. However due to the bandwidth of the USB 3.0 port used for the readout from our device to the computer, the maximum capacity for our single chip setup is 40×10^6 counts per second when using flat field illumination. If one electron lights up one pixel, this corresponds to a current of 6.4 pA which compared to conventional STEM imaging is somewhat on the low side. In the *Section 3*, it is shown that this estimate has to be adjusted with more technical details but the order of magnitude is correct [29]. In Fig. 1 (a), a schematic view of the setup is shown where an incoming convergent electron beam interacts with the sample. After the interaction with the sample, the electron beam propagates into the far field regime where the detector is placed. In Fig. 1 (b) an example of the data is shown where for every incoming event its point of impact and time of arrival (TOA) are saved. Knowing the probe position at each time, the conventional 4D STEM dataset can be obtained. In Fig. 1(c) some measured diffraction patterns are shown in which the sparsity is seen due to the low dose per scanned point. The resulting position averaged convergent beam electron diffraction (PACBED), calculated from the sum of all diffraction patterns, is also shown.

The Timepix3 detector was mounted on a probe-corrected FEI Themis Z using a custom designed retractable mount interface shown in Fig. 1 (d). In order to synchronize the scan coils with the detector, a custom scan engine is used [30, 31]. The detector and scan engine are synchronized by using a 10 MHz reference clock output which is then multiplied with a custom designed phase locked loop circuit to act as a 40 MHz master clock for the AdvAPIX in order to keep both scan engine and camera synchronised in time. At the start of the acquisition, a synchronisation signal is generated by the scan engine which triggers a recording sequence on the detector side. In this work, no flyback time is applied since we aim to reduce the dose as much as possible and we do not have access to a fast enough beam blaster to shut the beam down. Both the detector and scan engine have an application programming interface (API) in Python3 giving us the ability to automate the acquisition sequence. The incoming raw data from the detector is processed using self written software and the ptychographic reconstruction is performed using the single side band ptychography reconstruction

algorithm. The full recorded dataset and data processing software is made available in Zenodo allowing others to duplicate our efforts or to experiment with new algorithms that are optimised for event based data streams [32].

3. Timepix3 Characterization

The Timepix3 detector is a hybrid direct electron detector where the silicon sensor layer is bonded onto the underlying processing ASIC electronics similar to the Medipix chips [33, 34]. As for the Medipix detectors, the main parameter to be changed is the energy threshold which is a pre-set discrimination level used to discriminate an electron event above the noise floor. Hence, by varying this parameter we can select the amount of signal detected for a particular beam current. The energy threshold influences mainly two things, firstly the amount of detected events when one electron hits the detector and secondly the number of detected electrons. Throughout the rest of the paper the amount of pixels which are excited by a single electron will be referred to as a cluster. The identification of the clusters is derived from the work by van Schayck *et al.* [35] where clusters are identified by checking if neighbouring pixels are excited within a small time interval (~ 100 ns). The energy threshold also influences the number of detected electrons because increasing the threshold will result in some events remaining undetected since they do not exceed the threshold value when scattering inside the sensitive silicon layer.

The camera used in this work shows a workable calibrated threshold range between 7 and 33 keV, in *Supplementary Material S1* flat field images of different threshold values are shown where the artefacts for lower and higher threshold values are indicated. Note that these settings depend on an internal calibration routine that is performed when producing the detector.

In Fig. 2 (a), the cluster size as a function of energy threshold is plotted for 60 and 200 kV acceleration voltages. As expected, the cluster size decreases as a function of increasing energy threshold where for 200 kV the lowest cluster size is approximately 2.2 pixels and for 60 kV the size drops to 1 pixel at a threshold of 33 keV. In Fig. 2 (b), the detected electron current is shown as a function of energy threshold for the two acceleration voltages. The detected electron current is calculated by dividing the number of events on the detector by the cluster size within a fixed amount of time (two seconds in this experiment). From Fig. 2 (b), it is seen that at higher energy thresholds (33 keV) for 60 kV,

a significant amount of electrons (25 % at 33 keV) remain undetected. Since the incoming electron current is lower than the detection threshold for measuring the current via the fluorescent screen or spectrum drift tube method, no absolute measurement of the electron current could be performed here. However in the work of Krause *et al.* [29] it is shown that direct electron detectors provide an accurate estimate for low currents. Since the 7 keV threshold loses the least amount of electrons (see Fig. 2), this threshold is the most accurate measurement of the incoming electron count rate. Note that this is a lower boundary on the actual current since some electrons will backscatter and other electrons will scatter inside the silicon layer without exceeding the threshold energy. In the rest of this work, the total incoming electrons are calculated by dividing the number of detected events by the cluster size which is then multiplied by the ratio between the electron current at 7 keV and the used threshold value (see Fig. 2).

For example if 1×10^6 events per second are detected with a threshold of 30 keV at a 60 keV accelerating voltage, the incoming electron current is calculated by multiplying this value by $1/1.2$, the inverse of the cluster size, and 0.8, the ratio between the detector electron current at 7 and 30 keV.

From Fig. 2 we can conclude that at this lowest threshold, more electrons are detected but they make on average a larger cluster size reducing the maximum current on the detector. At 200 kV, the amount of events at the highest threshold (33 keV) is only 4% less compared than when using a threshold of 7 keV while it significantly reduces the cluster size. This results in a higher allowable beam current as compared to lower threshold levels since there is an upper limit on the maximum count rate of the detector

The detector was also briefly tested with an acceleration voltage of 300 kV. The cluster size increased quite considerably to an average of six pixels at a threshold of 33 keV. This meant that the incoming current should be dropped by a factor of three compared to 200 kV which makes the use of 300 keV electrons much less attractive and is therefore not considered further.

The identification of clusters can be used to increase the modulation transfer function (MTF) of the detector as shown in the work of van Schayck *et al.* [35] where they trained a neural network to better estimate the point of initial impact. However for our work such increasing of the MTF will not improve the results from our 4D STEM measurements since the algorithms used to reconstruct the signal are not sensitive to this [9, 14]. In *Supplementary Material S2*, the corrected electron signal, where the point of impact is calculated using

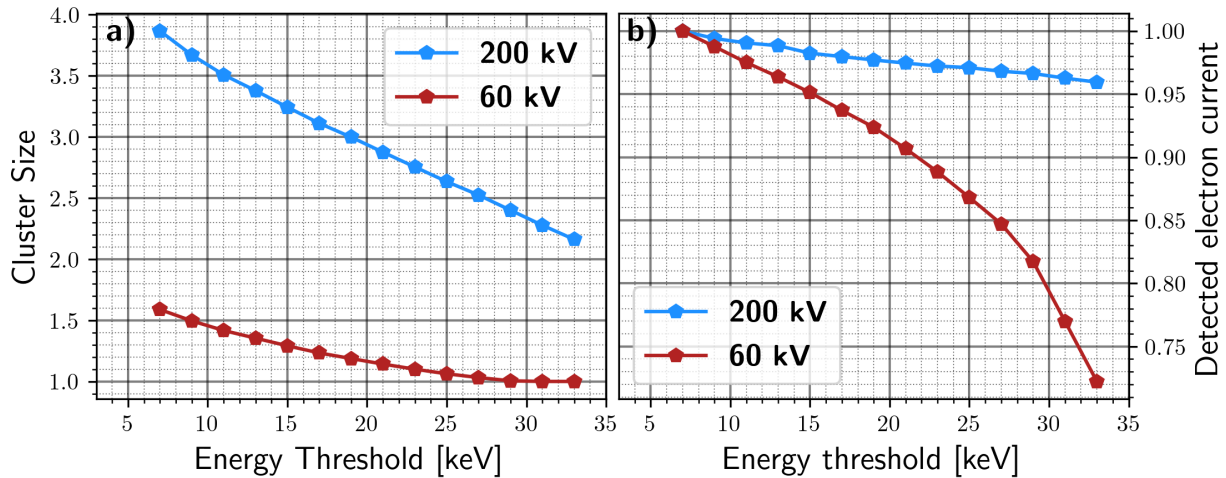


Figure 2: (a) The cluster size as a function of energy threshold for the two acceleration voltages 60 and 200 kV. (b) The detected electron current which is calculated by dividing the number of events on the detector by the cluster size. The detected current is relative compared to the detected current at a energy threshold of 7 keV.

mean x and y coordinate of the cluster, is used to investigate if the integrated center of Mass (iCOM) result changes due to this improvement of MTF. In *Supplementary Material S2* it is shown that a small discrepancy of approximately 1% between both reconstructed signals is observed. Therefore, when determining the positions of atoms and defects is the goal declustering is not necessary, but when the aim is to obtain a quantitative iCOM signal then declustering is likely desirable. During the experiments, it was noted that the detector does not record the incoming signal for short periods of time ranging from $50 \mu\text{s}$ to 1.75 ms. This happens for $\sim 0.12\%$ of the time that the detector is recording. This artefact is shown in *Supplementary Materials S3*. In this work we took the simple approach of replacing the integrated signal of a particular probe position, where the detector is not recording, by the average signal. In the future better ways of reconstructing these signals can be performed, and hopefully the losses fully avoided in the first place, but this is outside the scope of this work. Since the amount of lost electrons is relatively small, this artifact does not significantly hinder the performance of the camera.

4. Results & Discussion

A 2D WS_2 sample was used to showcase the performance of the detector at 60 kV. A multi-frame acquisition is performed where the probe, with a convergence angle of 25 mrad, is scanned over 1024×1024 probe positions three times at a dwell time of $6 \mu\text{s}$. The dose

per frame is estimated to be $6000 \text{ e}^- \text{ \AA}^{-2}$. The size of the dataset is 6.6 GB which is a significantly lower data storage requirement than using a 1-bit mode of an equivalently sized frame-based detector where the data size would be 33 GB.

In recent years, another type of data storage for frame based detector has been developed. The compression method is named electron-event representation (EER) which stores each electron-detection event as a tuple of position and time[36]. This is similar to the output of event based detectors. However the speed of the frame-based camera is still determined by the fps which is not the limit for the event based detectors [37, 38].

During the acquisition, the signal from the HAADF detector was read out simultaneously to collect the electrons which scatter to higher angles than the pixelated detector and provide a simultaneous Z-contrast image. In this work we provide three different signal reconstruction methods which are annular bright field (ABF), where only events which land on a annular ring on the detector is integrated from 33 to 100% relative to the convergence angle in order to obtain the image. Secondly, the iCOM signal is reconstructed from calculating the centre-of-mass of each probe position on which a two dimensional integration is performed which yields a scalar image. Finally, the single side-band (SSB) method is used to retrieve the phase of the object. The ABF and iCOM signals are calculated directly from the event list (see Fig. 1(b)) whereas for the SSB reconstruction the data was converted to standard non-sparse four-dimensional data for the most facile input to our existing

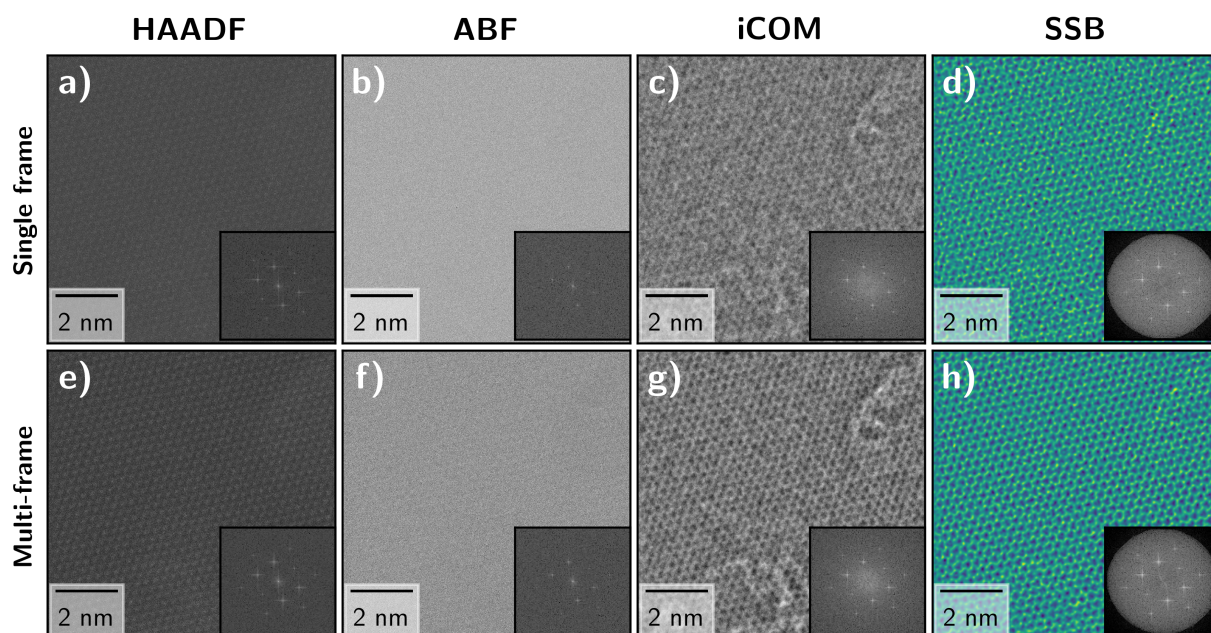


Figure 3: **(a,e)** Single and summed multi-frame HAADF images from a $3 \times 1024 \times 1024$ scan at $6 \mu\text{s}$ dwell time. The sample is a monolayer of WS_2 . The HAADF signal is collected with the conventional HAADF detector. **(b,f)** Single and multi-frame ABF images reconstructed from the simultaneously acquired 4D STEM dataset. **(c,g)** The reconstructed iCOM images from the single and multi-frame scans. **(d,h)** The reconstructed SSB images from the single and multi-frame scans.

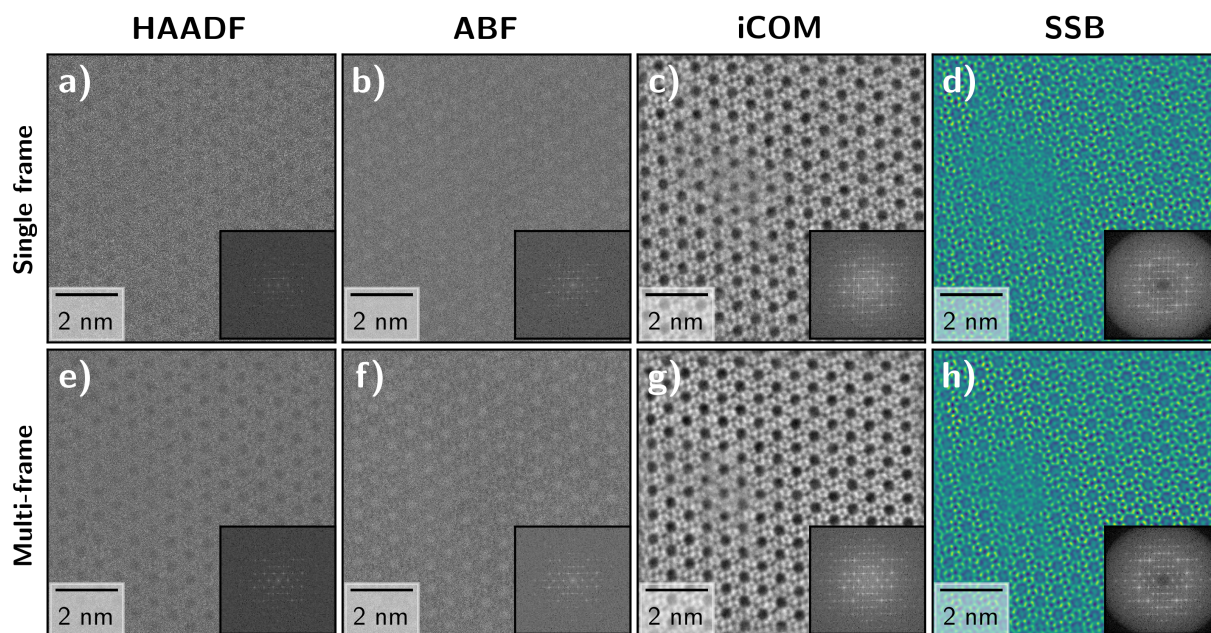


Figure 4: **(a,e)** Single and summed multi-frame HAADF images from a $1 \mu\text{s}$ dwell time $10 \times 1024 \times 1024$ scan of a silicalite-1 zeolite sample. **(b,f)** Single and summed multi-frame ABF images reconstructed from the use of virtual detector. **(c,g)** The reconstructed iCOM images from the single and multi-frame scans. On the left of the image the distortions due to finite response time of the scan coils are visible. **(d,h)** The reconstructed SSB images from the single and multi-frame scans.

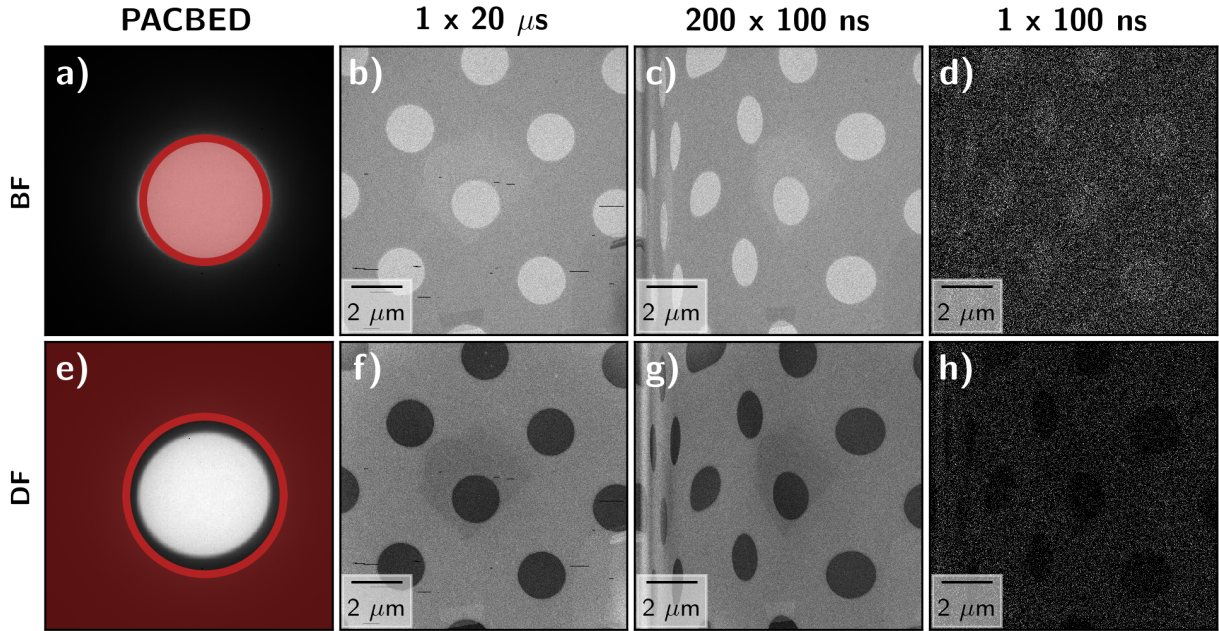


Figure 5: **(a,e)** The PACBED of the 4D STEM scan where, for both signals bright field (BF) and dark field (DF), the virtual detectors are shown. **(b,f)** The BF and DF signal of a 1024×1024 scan at $20 \mu\text{s}$ dwell time where the sample is a low magnification image a holey carbon film. **(c,g)** The summed BF and DF image of the same scan size with a dwell time of 100 ns and 200 frames which are scanned. Clear distortions arising from the response time of the coils are visible but the detector has no significant issues with this dwell time. **(d,h)** A single BF and DF frame of the fast scan using a dwell time of $1 \mu\text{s}$.

ptychographic processing software, which was written with framing cameras in mind. In the future the algorithms can be modified to accept the sparse event data directly or even perform ‘live’ imaging [38]. The resulting signals (ABF, iCOM and SSB) created from the 4D STEM images are shown in Fig. 3. The HAADF signal in Fig. 3(a,e) arises from the conventional HAADF detector (47-210 mrad) which we recorded in parallel with the event based detector data. The reconstructed multi-frame images are aligned using an open-source software which was developed for low signal-to-noise cryo-STEM data [39]. The software uses all possible combinations of image correlations, instead of using a single reference image, to determine the optimal shift. The relative image distortions between the scans are calculated using the SSB images due to its good contrast. The resulting images shifts were then also applied to the HAADF, ABF and iCOM images to align them. In Fig. 3(b,f) the ABF signal is shown where the low contrast arises as a result from the low dose conditions. This is not particularly surprising as in the weak phase object approximation (WPOA) zero contrast is expected when using a centrosymmetric detector configuration, and the 2D WS_2 is of course thin, relatively weak and lacking

in channeling contrast in comparison to typical 3D materials [6].

The iCOM signal shown in Fig. 3(d,h) and the SSB ptychographic reconstruction shown in Fig. 3(c,g) both take greater advantage of the 4D data and show much stronger signals. The difference in contrast of the SSB with respect to the iCOM signal arises from the different contrast transfer functions (CTF) of both signals [8, 40] and the way in which the ptychographic method keeps track explicitly of where in probe reciprocal space each frequency is transferred [6, 9]. The lower limit of the electron dose is calculated using the information from Fig. 2 (b) where the experiment was performed at an energy threshold of 30 keV indicating that minimally $\sim 25\%$ of the incoming electrons are not detected. This gives a minimum dose of $\sim 6000 \text{ e}^- \text{ \AA}^{-2}$ per frame. The same type of data acquisition at 60 kV can be performed at 200 kV where the main difference is the larger cluster size at 200 kV. However in terms of lost electrons, the 200 kV is better since only a small fraction (3%) seems to be lost by increasing the energy threshold to the 31 keV used for the 200 kV data presented here taken of a silicalite-1 zeolite [41]. A $10 \times 1024 \times 1024$ probe position scan is performed at a dwell time of $1 \mu\text{s}$

where the dose per frame was $300 \text{ e}^- \text{ \AA}^{-2}$ and the total dose over the ten scans was $3000 \text{ e}^- \text{ \AA}^{-2}$. The convergence angle used during the experiment was 12 mrad. In Fig. 4, the reconstructed signals are shown where the HAADF and ABF shows, as expected, very low contrast. As for the WS_2 , the iCOM and SSB signals both show good contrast. The distortions visible on the left of the images are due to the slow response of the scan coils at this dwell time as we have no flyback time.

To check if we were able to record 4D STEM scans at dwell times of 100 ns and that the detector is still able to record a proper 4D STEM dataset, a low magnification scan on a holey carbon film was performed. This sample and magnification was selected to have a high contrast and to minimize the effect of drift since the individual 100 ns scans have such a low signal-to-noise that aligning them would be very challenging and beyond the scope of the present study. First a 1024×1024 scan at a $20 \mu\text{s}$ dwell time was performed, the bright field (BF) and dark field (DF) images are shown in Fig. 5(b,f). The virtual detectors used to reconstruct the signal are shown in Fig. 5(a,e) where the BF signal arises from the integration over the entire central beam and the DF collects all the signal which lands outside the central beam. Further the same field of view is scanned with the same number of probe positions except the dwell time is decreased to 100 ns where a total of 200 frames were scanned to have an equal dose as the slower $20 \mu\text{s}$ scan. The resulting summed BF and DF are shown in Fig. 5(c,g). Large distortions due to the finite response of the scan coils are visible but in essence, the 4D STEM signal is recorded properly showing that the detector can handle such short dwell times with ease. In Fig. 5(d,h) the BF and DF of a single scan are shown where the low signal-to-noise results from the very small number of counts per probe position. These results show that even shorter dwell times would be possible if the scanning system bandwidth could be improved, possibly at the expense of maximum field of view capabilities. Efforts in this direction are reported for magnetic deflection [42] but also electrostatic deflection coupled to high bandwidth amplifiers are a possibility.

Due to the speed at which full 4D STEM data sets can now be recorded with event based detectors, this technique has the capability to be combined with other conventional high resolution STEM (HR-STEM) methods. For instance, tomographic series can be performed where instead of just the HAADF signal, the full diffraction pattern can be recorded where a large range of scattering angles is available. In the post-processing steps, different signals can be reconstructed to increase the information gathered from the experiment [43] with the

potential for even online processing of the datastream [44].

Another method that becomes more attractive for 4D STEM is depth sectioning where instead of the simple fixed focus multi-frame acquisition used in this work, between each frame the focus is changed in order to get three dimensional information about sample [45, 46, 47, 48, 49]. Adding the 4D STEM dataset to such optical sectioning could potentially improve its performance where for instance for S-matrix reconstruction this depth sectioning is necessary [50]. Finally, acquiring 4D STEM data when the scan sequence is changed is easily accessible if one knows at each time where the probe is positioned. These different scanning strategies are used e.g. to decrease damage [51, 52], or distortions [53, 54].

Although the main limit of the current Timepix3 camera is its limited dose rate, new plans for a Timepix4 chip have been revealed where the number of pixels almost quadruples to 512×448 and the maximum dose rate increases with a factor of six. This allows for a current increase by approximately a factor of 24, bringing it, in the coming years, much more in line with conventional beam currents used in STEM imaging [55].

5. Conclusion

In this work, it is shown that using a hybrid pixel direct electron event based detector rather than conventional frame-based cameras enables the recording of 4D STEM datasets with dwell times as low as 100 ns. The detector was characterised at two different acceleration voltages, 60 and 200 kV. For 200 kV, the maximum electron count rate is half that of 60 kV. However when increasing the threshold for 60 kV, a significant decrease in collection efficiency is observed. Hence when performing experiments, a compromise on the threshold is required where the higher the threshold, the higher the electron dose rate that can be detected. However this decreases the collection efficiency which is detrimental for beam sensitive materials. Furthermore by synchronizing the detector with a versatile scan engine, multi-frame 4D STEM acquisitions could be performed with scan sizes of 1024×1024 or larger using dwell times in the order of μs . This opens up the possibility to always perform 4D STEM acquisition instead of conventional STEM and profit from the significantly higher information content about the sample for the same incoming beam current. In the future, we anticipate improvements in both the data processing times and the maximum count rates detectable by event based detectors to make this type of setup more straightforward.

Acknowledgements

This project has received funding from the European Union's Horizon 2020 Research Infrastructure - Integrating Activities for Advanced Communities under grant agreement No 823717 – ESTEEM3. J.V. and A.B. acknowledge funding from FWO project G093417N ('Compressed sensing enabling low dose imaging in transmission electron microscopy'). J.V. and D.J. acknowledge funding from FWO project G042920N 'Coincident event detection for advanced spectroscopy in transmission electron microscopy'. We acknowledge funding under the European Union's Horizon 2020 research and innovation programme (J.V. and D.J. under grant agreement No 101017720, FET-Proactive EBEAM, and C.H., C.G., X.X. and T.J.P. from the European Research Council (ERC) Grant agreement No. 802123-HDEM).

All data discussed in this manuscript is openly available through Zenodo to stimulate further research on this topic and to improve reproducibility.

References

- [1] S. Procz, C. Avila, J. Fey, G. Roque, M. Schuetz, E. Hamann, X-ray and gamma imaging with medipix and timepix detectors in medical research 127 106104. doi:10.1016/j.radmeas.2019.04.007. URL <https://linkinghub.elsevier.com/retrieve/pii/S1350448719300599>
- [2] B. Bergmann, P. Burian, P. Manek, S. Pospisil, 3d reconstruction of particle tracks in a 2 mm thick CdTe hybrid pixel detector 79 (2) 165. doi:10.1140/epjc/s10052-019-6673-z. URL <http://link.springer.com/10.1140/epjc/s10052-019-6673-z>
- [3] W. Kuhlbrandt, The resolution revolution 343 (6178) 1443–1444. doi:10.1126/science.1251652. URL <https://www.sciencemag.org/lookup/doi/10.1126/science.1251652>
- [4] B. E. Bammes, R. H. Rochat, J. Jakana, D.-H. Chen, W. Chiu, Direct electron detection yields cryo-EM reconstructions at resolutions beyond 3/4 nyquist frequency 177 (3) 589–601. doi:10.1016/j.jsb.2012.01.008. URL <https://linkinghub.elsevier.com/retrieve/pii/S1047847712000287>
- [5] C. Ophus, Four-dimensional scanning transmission electron microscopy (4d-STEM): From scanning nanodiffraction to ptychography and beyond 25 (3) 563–582. doi:10.1017/S1431927619000497. URL https://www.cambridge.org/core/product/identifier/S1431927619000497/type/journal_article
- [6] T. J. Pennycook, A. R. Lupini, H. Yang, M. F. Murfitt, L. Jones, P. D. Nellist, Efficient phase contrast imaging in STEM using a pixelated detector. part I: Experimental demonstration at atomic resolution 151 160–167. doi:10.1016/j.ultramic.2014.09.013. URL <https://linkinghub.elsevier.com/retrieve/pii/S0304399114001934>
- [7] J. A. Hachtel, J. C. Idrobo, M. Chi, Sub-Ångstrom electric field measurements on a universal detector in a scanning transmission electron microscope 4 (1) 10. doi:10.1186/s40679-018-0059-4. URL <https://ascimaging.springeropen.com/articles/10.1186/s40679-018-0059-4>
- [8] I. Lazić, E. G. Bosch, S. Lazar, Phase contrast STEM for thin samples: Integrated differential phase contrast 160 265–280. doi:10.1016/j.ultramic.2015.10.011. URL <https://linkinghub.elsevier.com/retrieve/pii/S0304399115300449>
- [9] H. Yang, T. J. Pennycook, P. D. Nellist, Efficient phase contrast imaging in STEM using a pixelated detector. part II: Optimisation of imaging conditions 151 232–239. doi:10.1016/j.ultramic.2014.10.013. URL <https://linkinghub.elsevier.com/retrieve/pii/S0304399114002058>
- [10] T. J. Pennycook, G. T. Martinez, P. D. Nellist, J. C. Meyer, High dose efficiency atomic resolution imaging via electron ptychography 196 131–135. doi:10.1016/j.ultramic.2018.10.005. URL <https://linkinghub.elsevier.com/retrieve/pii/S0304399118302316>
- [11] K. Müller-Caspary, M. Duchamp, M. Rösner, V. Migunov, F. Winkler, H. Yang, M. Huth, R. Ritz, M. Simson, S. Ihle, H. Soltau, T. Wehling, R. E. Dunin-Borkowski, S. Van Aert, A. Rosenauer, Atomic-scale quantification of charge densities in two-dimensional materials 98 (12) 121408. doi:10.1103/PhysRevB.98.121408. URL <https://link.aps.org/doi/10.1103/PhysRevB.98.121408>
- [12] G. T. Martinez, T. C. Naginey, L. Jones, C. M. O'Leary, T. J. Pennycook, R. J. Nicholls, J. R. Yates, P. D. Nellist, Direct imaging of charge redistribution due to bonding at atomic resolution via electron ptychography arXiv:1907.12974. URL <http://arxiv.org/abs/1907.12974>
- [13] J. Madsen, T. J. Pennycook, T. Susi, ab initio description of bonding for transmission electron microscopy 113253 doi:10.1016/j.ultramic.2021.113253. URL <https://linkinghub.elsevier.com/retrieve/pii/S0304399121000449>
- [14] K. Müller-Caspary, F. F. Krause, F. Winkler, A. Béché, J. Verbeeck, S. Van Aert, A. Rosenauer, Comparison of first moment STEM with conventional differential phase contrast and the dependence on electron dose 203 95–104. doi:10.1016/j.ultramic.2018.12.018. URL <https://linkinghub.elsevier.com/retrieve/pii/S0304399118302730>
- [15] J. Mir, R. Clough, R. MacInnes, C. Gough, R. Plackett, I. Shipsey, H. Sawada, I. MacLaren, R. Ballabriga, D. Maneuski, V. O'Shea, D. McGrouther, A. Kirkland, Characterisation of the medipix3 detector for 60 and 80 keV electrons 182 44–53. doi:10.1016/j.ultramic.2017.06.010. URL <https://linkinghub.elsevier.com/retrieve/pii/S0304399116303989>
- [16] H. Ryll, M. Simson, R. Hartmann, P. Holl, M. Huth, S. Ihle, Y. Kondo, P. Kotula, A. Liebel, K. Müller-Caspary, A. Rosenauer, R. Sagawa, J. Schmidt, H. Soltau, L. Strüder, A pnCCD-based, fast direct single electron imaging camera for TEM and STEM 11 (4) P04006–P04006. doi:10.1088/1748-0221/11/04/P04006. URL <http://stacks.iop.org/1748-0221/11/i=04/a=P04006?key=crossref.341dff1a30df71a36812e65192e3f0f7>
- [17] C. M. O'Leary, C. S. Allen, C. Huang, J. S. Kim, E. Liberti, P. D.

- Nellist, A. I. Kirkland, Phase reconstruction using fast binary 4d STEM data 116 (12) 124101. doi:10.1063/1.5143213. URL <http://aip.scitation.org/doi/10.1063/1.5143213>
- [18] J. Ciston, I. J. Johnson, B. R. Draney, P. Ercius, E. Fong, A. Goldschmidt, J. M. Joseph, J. R. Lee, A. Mueller, C. Ophus, A. Selvarajan, D. E. Skinner, T. Stezelberger, C. S. Tindall, A. M. Minor, P. Denes, The 4d camera: Very high speed electron counting for 4d-STEM 25 1930–1931. doi:10.1017/S1431927619010389. URL https://www.cambridge.org/core/product/identifier/S1431927619010389/type/journal_article
- [19] P. Ercius, I. Johnson, H. Brown, P. Pelz, S.-L. Hsu, B. Draney, E. Fong, A. Goldschmidt, J. Joseph, J. Lee, J. Ciston, C. Ophus, M. Scott, A. Selvarajan, D. Paul, D. Skinner, M. Hanwell, C. Harris, P. Avery, T. Stezelberger, C. Tindall, R. Ramesh, A. Minor, P. Denes, The 4d camera – an 87 kHz frame-rate detector for counted 4d-STEM experiments 26 1896–1897. doi:10.1017/S1431927620019753. URL https://www.cambridge.org/core/product/identifier/S1431927620019753/type/journal_article
- [20] J. Song, C. S. Allen, S. Gao, C. Huang, H. Sawada, X. Pan, J. Warner, P. Wang, A. I. Kirkland, Atomic resolution defocused electron ptychography at low dose with a fast, direct electron detector 9 (1) 3919. doi:10.1038/s41598-019-40413-z. URL <http://www.nature.com/articles/s41598-019-40413-z>
- [21] Z. Chen, M. Odstreil, Y. Jiang, Y. Han, M.-H. Chiu, L.-J. Li, D. A. Muller, Mixed-state electron ptychography enables sub-angstrom resolution imaging with picometer precision at low dose 11 (1) 2994. doi:10.1038/s41467-020-16688-6. URL <http://www.nature.com/articles/s41467-020-16688-6>
- [22] L. Zhou, J. Song, J. S. Kim, X. Pei, C. Huang, M. Boyce, L. Mendonça, D. Clare, A. Siebert, C. S. Allen, E. Liberti, D. Stuart, X. Pan, P. D. Nellist, P. Zhang, A. I. Kirkland, P. Wang, Low-dose phase retrieval of biological specimens using cryo-electron ptychography 11 (1) 2773. doi:10.1038/s41467-020-16391-6. URL <http://www.nature.com/articles/s41467-020-16391-6>
- [23] J. Rodenburg, B. McCallum, P. Nellist, Experimental tests on double-resolution coherent imaging via STEM 48 (3) 304–314. doi:10.1016/0304-3991(93)90105-7. URL <https://linkinghub.elsevier.com/retrieve/pii/0304399193901057>
- [24] The theory of super-resolution electron microscopy via wigner-distribution deconvolution 339 (1655) 521–553. doi:10.1098/rsta.1992.0050. URL <https://royalsocietypublishing.org/doi/10.1098/rsta.1992.0050>
- [25] H. Yang, R. N. Rutte, L. Jones, M. Simson, R. Sagawa, H. Ryll, M. Huth, T. J. Pennycook, M. Green, H. Soltau, Y. Kondo, B. G. Davis, P. D. Nellist, Simultaneous atomic-resolution electron ptychography and z-contrast imaging of light and heavy elements in complex nanostructures 7 (1) 12532. doi:10.1038/ncomms12532. URL <http://www.nature.com/articles/ncomms12532>
- [26] P. Hatfield, W. Furnell, A. Shenoy, E. Fox, R. Parker, L. Thomas, The LUCID-timepix spacecraft payload and the CERN@school educational programme 13 (10) C10004–C10004. doi:10.1088/1748-0221/13/10/C10004. URL <https://iopscience.iop.org/article/10.1088/1748-0221/13/10/C10004>
- [27] R. Beacham, A. M. Raighne, D. Maneuski, V. O’Shea, S. McVitie, D. McGrouther, Medipix2/timepix detector for time resolved transmission electron microscopy 6 (12) C12052–C12052. doi:10.1088/1748-0221/6/12/C12052. URL <https://iopscience.iop.org/article/10.1088/1748-0221/6/12/C12052>
- [28] Advacam advapix TPX3. URL <https://advacam.com/camera/advapix-tpx3>
- [29] F. F. Krause, M. Schowalter, O. Oppermann, D. Marquardt, K. Müller-Caspary, R. Ritz, M. Simson, H. Ryll, M. Huth, H. Soltau, A. Rosenauer, Precise measurement of the electron beam current in a TEM 223 113221. doi:10.1016/j.ultramic.2021.113221. URL <https://linkinghub.elsevier.com/retrieve/pii/S0304399121000164>
- [30] A. Zobelli, S. Y. Woo, A. Tararan, L. H. Tizei, N. Brun, X. Li, O. Stéphan, M. Kociak, M. Tencé, Spatial and spectral dynamics in STEM hyperspectral imaging using random scan patterns 112912doi:10.1016/j.ultramic.2019.112912. URL <https://linkinghub.elsevier.com/retrieve/pii/S0304399119303110>
- [31] Attolight. URL <https://attolight.com/>
- [32] D. Jannis, C. Hofer, C. Gao, X. Xie, A. Beche, T. Pennycook, J. Verbeeck, Event driven 4d STEM acquisition with a timepix3 detector: microsecond dwelltime and faster scans for high precision and low dose applicationsPublisher: Zenodo. doi:10.5281/zenodo.5068510.
- [33] A. Rosenfeld, M. Silari, M. Campbell, The editorial 139 106483. doi:10.1016/j.radmeas.2020.106483. URL <https://linkinghub.elsevier.com/retrieve/pii/S1350448720302596>
- [34] R. Ballabriga, M. Campbell, X. Llopart, Asic developments for radiation imaging applications: The medipix and timepix family 878 10–23. doi:10.1016/j.nima.2017.07.029. URL <https://linkinghub.elsevier.com/retrieve/pii/S0168900217307714>
- [35] J. P. van Schayck, E. van Genderen, E. Maddox, L. Roussel, H. Boulanger, E. Fröjdh, J.-P. Abrahams, P. J. Peters, R. B. Ravelli, Sub-pixel electron detection using a convolutional neural network 218 113091. doi:10.1016/j.ultramic.2020.113091. URL <https://linkinghub.elsevier.com/retrieve/pii/S0304399120302424>
- [36] H. Guo, E. Franken, Y. Deng, S. Benlekbir, G. Singla Lezcano, B. Janssen, L. Yu, Z. A. Ripstein, Y. Z. Tan, J. L. Rubinstein, Electron-event representation data enable efficient cryoEM file storage with full preservation of spatial and temporal resolution 7 (5) 860–869. doi:10.1107/S205225252000929X. URL <https://scripts.iucr.org/cgi-bin/paper?S205225252000929X>
- [37] A. Datta, K. F. Ng, D. Balakrishnan, M. Ding, S. W. Chee, Y. Ban, J. Shi, N. D. Loh, A data reduction and compression description for high throughput time-resolved electron microscopy 12 (1) 664. doi:10.1038/s41467-020-20694-z. URL <http://www.nature.com/articles/s41467-020-20694-z>
- [38] P. M. Pelz, I. Johnson, C. Ophus, P. Ercius, M. C. Scott, Real-time interactive 4d-STEM phase-contrast imaging from electron event representation dataarXiv:2104.06336. URL <http://arxiv.org/abs/2104.06336>
- [39] B. H. Savitzky, I. El Baggari, C. B. Clement, E. Waite, B. H. Goodge, D. J. Baek, J. P. Sheckelton, C. Pasco, H. Nair, N. J. Schreiber, J. Hoffman, A. S. Admasu, J. Kim,

- S.-W. Cheong, A. Bhattacharya, D. G. Schlom, T. M. McQueen, R. Hovden, L. F. Kourkoutis, Image registration of low signal-to-noise cryo-STEM data 191 56–65. doi:10.1016/j.ultramic.2018.04.008. URL <https://linkinghub.elsevier.com/retrieve/pii/S0304399117304369>
- [40] C. M. O’Leary, G. T. Martinez, E. Liberti, M. J. Humphry, A. I. Kirkland, P. D. Nellist, Contrast transfer and noise considerations in focused-probe electron ptychography 221 113189. doi:10.1016/j.ultramic.2020.113189. URL <https://linkinghub.elsevier.com/retrieve/pii/S0304399120303314>
- [41] S. Fujiyama, K. Yoza, N. Kamiya, K. Nishi, Y. Yokomori, Entrance and diffusion pathway of CO₂ and dimethyl ether in silicalite-1 zeolite channels as determined by single-crystal XRD structural analysis 71 (1) 112–118. doi:10.1107/S2052520615000256. URL <http://scripts.iucr.org/cgi-bin/paper?S2052520615000256>
- [42] R. Ishikawa, Y. Jimbo, M. Terao, M. Nishikawa, Y. Ueno, S. Morishita, M. Mukai, N. Shibata, Y. Ikuhara, High spatiotemporal-resolution imaging in the scanning transmission electron microscope 69 (4) 240–247. doi:10.1093/jmicro/dfa017. URL <https://academic.oup.com/jmicro/article/69/4/240/5815181>
- [43] D. J. Chang, D. S. Kim, A. Rana, X. Tian, J. Zhou, P. Ercius, J. Miao, Ptychographic atomic electron tomography: Towards three-dimensional imaging of individual light atoms in materials 102 (17) 174101. doi:10.1103/PhysRevB.102.174101. URL <https://link.aps.org/doi/10.1103/PhysRevB.102.174101>
- [44] A. Clausen, D. Weber, K. Ruzaeva, V. Migunov, A. Baburajan, A. Bahuleyan, J. Caron, R. Chandra, S. Dey, S. Halder, D. S. Katz, B. D. Levin, M. Nord, C. Ophus, S. Peter, J. Schyndel van, J. Shin, S. Sunku, K. Müller-Caspary, R. E. Dunin-Borkowski, LiberTEM/LiberTEM: 0.7.0. doi:10.5281/ZENODO.4923277. URL <https://zenodo.org/record/4923277>
- [45] K. van Benthem, A. R. Lupini, M. Kim, H. S. Baik, S. Doh, J.-H. Lee, M. P. Oxley, S. D. Findlay, L. J. Allen, J. T. Luck, S. J. Pennycook, Three-dimensional imaging of individual hafnium atoms inside a semiconductor device 87 (3) 034104. doi:10.1063/1.1991989. URL <http://aip.scitation.org/doi/10.1063/1.1991989>
- [46] R. Ishikawa, S. J. Pennycook, A. R. Lupini, S. D. Findlay, N. Shibata, Y. Ikuhara, Single atom visibility in STEM optical depth sectioning 109 (16) 163102. doi:10.1063/1.4965709. URL <http://aip.scitation.org/doi/10.1063/1.4965709>
- [47] H. L. Xin, D. A. Muller, Aberration-corrected ADF-STEM depth sectioning and prospects for reliable 3d imaging in s/TEM 58 (3) 157–165. doi:10.1093/jmicro/dfn029. URL <https://academic.oup.com/jmicro/article-lookup/doi/10.1093/jmicro/dfn029>
- [48] T. J. Pennycook, H. Yang, L. Jones, M. Cabero, A. Rivera-Calzada, C. Leon, M. Varela, J. Santamaria, P. D. Nellist, 3d elemental mapping with nanometer scale depth resolution via electron optical sectioning 174 27–34. doi:10.1016/j.ultramic.2016.12.002. URL <https://linkinghub.elsevier.com/retrieve/pii/S0304399116303631>
- [49] H. Yang, J. G. Lozano, T. J. Pennycook, L. Jones, P. B. Hirsch, P. D. Nellist, Imaging screw dislocations at atomic resolution by aberration-corrected electron optical sectioning 6 (1) 7266. doi:10.1038/ncomms8266. URL <http://www.nature.com/articles/ncomms8266>
- [50] P. M. Pelz, H. G. Brown, J. Ciston, S. D. Findlay, Y. Zhang, M. Scott, C. Ophus, Reconstructing the scattering matrix from scanning electron diffraction measurements alone arXiv:2008.12768. URL <http://arxiv.org/abs/2008.12768>
- [51] A. Velazco, D. Jannis, A. Béché, J. Verbeeck, Reducing electron beam damage through alternative STEM scanning strategies. part i – experimental findings arXiv:2105.01617. URL <http://arxiv.org/abs/2105.01617>
- [52] D. Nicholls, J. Lee, H. Amari, A. J. Stevens, B. L. Mehdi, N. D. Browning, Minimising damage in high resolution scanning transmission electron microscope images of nanoscale structures and processes 12 (41) 21248–21254. doi:10.1039/D0NR04589F. URL <http://xlink.rsc.org/?DOI=D0NR04589F>
- [53] X. Sang, A. R. Lupini, R. R. Unocic, M. Chi, A. Y. Borisevich, S. V. Kalinin, E. Endeve, R. K. Archibald, S. Jesse, Dynamic scan control in STEM: spiral scans 2 (1) 6. doi:10.1186/s40679-016-0020-3. URL <https://ascimaging.springeropen.com/articles/10.1186/s40679-016-0020-3>
- [54] A. Velazco, M. Nord, A. Béché, J. Verbeeck, Evaluation of different rectangular scan strategies for STEM imaging 215 113021. doi:10.1016/j.ultramic.2020.113021. URL <https://linkinghub.elsevier.com/retrieve/pii/S0304399120300334>
- [55] Xavier Llopart, Timepix4 detectors. URL https://indico.cern.ch/event/876275/contributions/3729426/attachments/1986038/3309319/Xavi_Timepix4_Muon.pdf

6. Supplementary Material

S1. Energy threshold variation for flat field illumination

In Fig 6, the average cluster size as a function of threshold is shown. At low thresholds from 1-5 keV the cluster size decreases with decreasing threshold. This might seem nonphysical since the lower the threshold the larger the cluster size induced by an electron hit should be. However, one possible explanation for this effect would be that at low thresholds ≤ 5 keV thermal noise or other types of random noise start to be detected resulting in a smaller average cluster size since the average cluster size of random noise is one, although we note that at 1 kV the grid pattern artefact that appears in the flat field images is likely due to the underlying detector geometry. The results of flat field illumination of the incoming electron beam at 60 and 200 kV accelerating voltages are shown in Fig. 7 and 8 as a function of the threshold voltage. In order to remove the influence of such noise, the minimum usable threshold was determined to be at 7 keV. From Fig. 7 and 8, a maximum value of the threshold is determined by investigating the number of dead pixels as a function of threshold. A dead pixel is defined as a pixel which is not giving any counts during the acquisition. At 35 keV a sharp increase in the number of dead pixels is seen making higher threshold values undesirable for the experiments. Therefore the valid range of thresholds is determined to be between 7 and 33 keV.

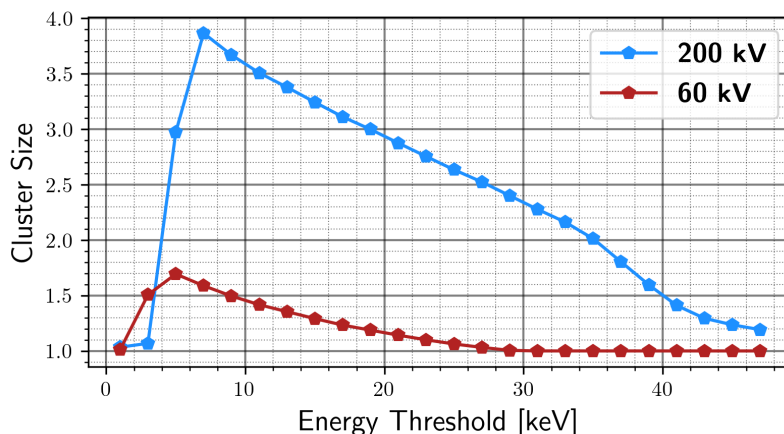


Figure 6: The average cluster size calculated as a function of threshold for 60 and 200 kV accelerating voltages.

S2. Raw vs declustered 4D STEM dataset

In this section, we investigate if the clustering of the electron events has a significant influence on the reconstructed integrated centre-of-mass (iCOM) signal. An electron probe was scanned with a $6 \mu\text{s}$ dwell time over 1024×1024 points of a zeolite silicalite-1 sample at a 200 kV accelerating voltage. The declustering algorithm searches for adjacent pixels which are excited within a time interval of 100 ns [35]. From this cluster the new corrected time-of-arrival (TOA) is when the first pixel of the cluster is excited. The point of impact is calculated using the centre-of-mass of the cluster. In Fig. 9 (a,b), respectively the raw and declustered reconstructed iCOM images are shown and seen to be very similar. The difference between the two signals is shown in Fig. 9 (c), showing that for iCOM the reduction of modulation transfer function (MTF) has no visual influence on the result. The average value of the difference is 1%. Hence when the iCOM signal is used to extract atomic positions, declustering will not greatly improve the data quality. However, when quantitative information is desired from the iCOM signal, declustering is expected to improve the results. In Fig. 9(d), 500 events collected sequentially from the dataset are shown from which the clusters are clearly visible. In (e), the corrected events are shown with the estimated points of impact of the electrons. In the inset figures the position averaged convergent beam electron diffraction (PACBED) of both raw and declustered datasets are shown in which also no clear difference is observed.

60 kV

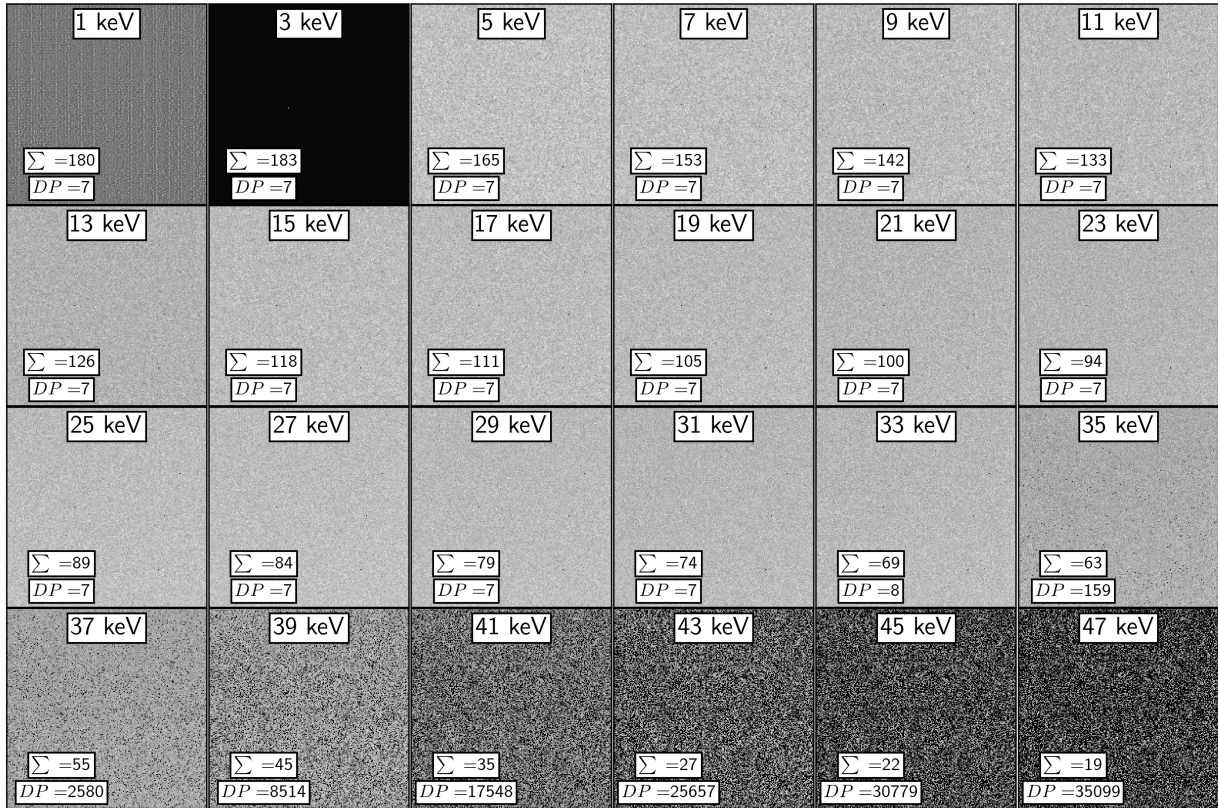


Figure 7: The flat field illumination of 60 kV electrons where the threshold is varied. The relative total number of detected electrons compared to 21 keV in percentage is shown and also the number of dead pixels is indicated in the plots.

S3. Artefacts in Timepix3 data

When recording a data stream we find that sometimes the camera does not record the incoming electrons for certain time periods ranging from $50 \mu\text{s}$ to 1.75 ms . To investigate this, the dataset of the low magnification scan used for Fig. 5 of the main text is used. In Fig. 10 (a), a histogram calculated from the TOA of the incoming events with a bin size of $10 \mu\text{s}$ is shown. This shows the number of events where at some particular times, the counts drop unphysically to zero. The time that the camera is down for this acquisition is 0.12% , which is a relatively small proportion of time compared to the entire acquisition. In Fig. 10 (b), the corresponding dark field (DF) image is shown where the virtual detector region is shown in Fig. 5. The black lines on the image are due to the artefacts. In this work a very simple method is used to mitigate the artefacts by filling these pixels with the average value of the image. While this is likely not the best way to reconstruct the images, this is beyond the scope of our present work. In the future we expect other improved methods for image restoration or ideally ways to avoid the artefacts in the first place can be developed.

200 kV

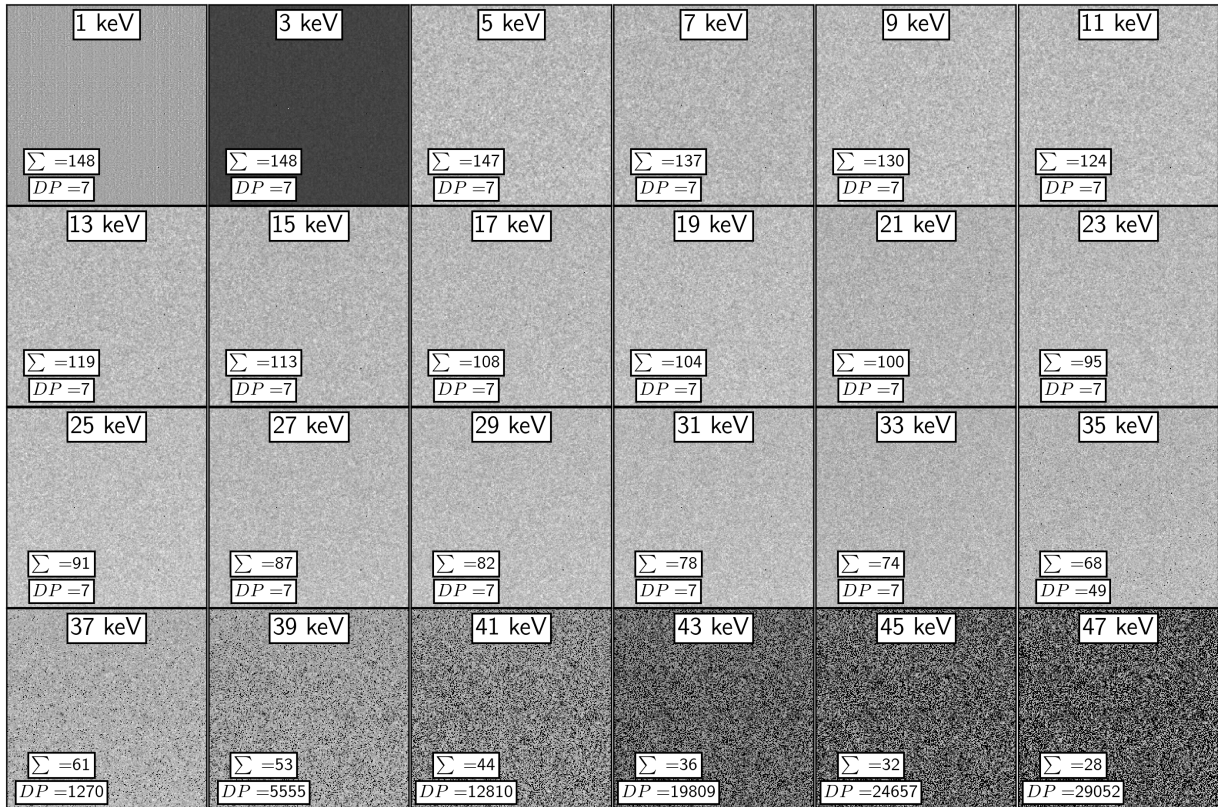


Figure 8: The flat field illumination of 200 kV electrons where the threshold is varied. The relative total number of detected electrons compared to 21 keV in percentage is shown and also the number of dead pixels is indicated in the plots.

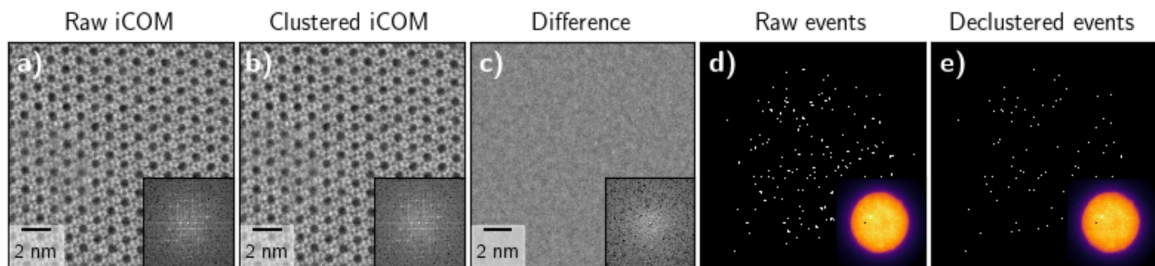


Figure 9: **(a)** The reconstructed iCOM image of the raw dataset from a silicalite-1 zeolite. The scan size is 1024×1024 , the dwell time is $6 \mu\text{s}$, and the acceleration voltage is 200 kV. In the insets the Fourier transform of the iCOM signal is shown. **(b)** The same as (a) except declustering is applied. **(c)** The difference between (a) and (b) showing the similarity between the two signals. **(d)** a set of 500 sequential events from the same dataset detected on the Timepix3 camera, in which the clustering of event is clearly seen. In the inset the PACBED pattern is shown. **(e)** The same as (d) but now with declustering applied.

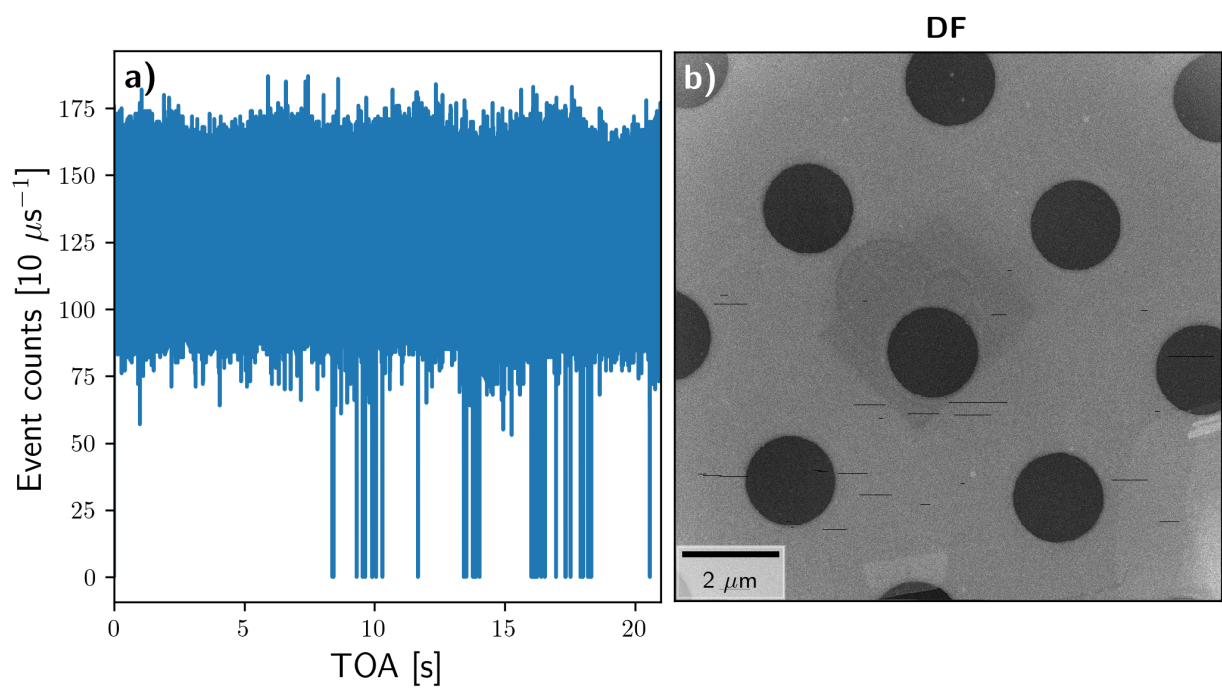


Figure 10: **(a)** A histogram of the TOA of the incoming events with a bin size of $10 \mu\text{s}$. **(b)** The reconstructed DF signal where the dark lines correspond to the artefacts which arise when the detector does not detect signal in some time windows.